

## Article

# Research on the Reinforcement and Inhibition of Water–Salt Activity in Mural Ground Layers by Superhydrophobic SiO<sub>2</sub> Particles

Qixing Xia <sup>1,2,3,\*</sup> and Wenqiang Dong <sup>1,2,3,\*</sup><sup>1</sup> Institute of Culture and Heritage, Northwestern Polytechnical University, Xi'an 710072, China<sup>2</sup> Key Scientific Research Base of the State Administration of Cultural Heritage for the Conservation and Restoration of Murals and Material Science Research, Northwestern Polytechnical University, Xi'an 710072, China<sup>3</sup> Key Laboratory of Archaeological Exploration and Cultural Heritage Conservation Technology (Northwestern Polytechnical University), Ministry of Education, Xi'an 710129, China

\* Correspondence: xqixing@nwpu.edu.cn (Q.X.); dongwq@nwpu.edu.cn (W.D.)

**Abstract:** Due to notable water–salt activities, salt damage easily recurs and becomes one of the biggest challenges for the protection of ancient murals. Herein, superhydrophobic SiO<sub>2</sub> materials with different sizes were used to modify mural ground layer substrates, and the improvement effect mechanisms were systematically evaluated with scanning electron microscopy (SEM), X-ray diffraction (XRD), laser scanning confocal microscopy (LSCM), and a contact angle instrument. The results show that the superhydrophobic SiO<sub>2</sub> can spread into the substrates through holes and cracks and further increase the contact angles of the substrates to water droplets. Compared with the initial ground layer substrate, the substrates treated with the superhydrophobic SiO<sub>2</sub> possess stronger mechanical strength and a better ability in suppressing water–salt activity. In particular, larger-size SiO<sub>2</sub> (mSiO<sub>2</sub>) maintains better mechanical reinforcement in the substrates, because mSiO<sub>2</sub> can provide better support in the internal gaps of the substrates. By contrast, nSiO<sub>2</sub> can spread deeper into the substrate than mSiO<sub>2</sub>, and more greatly improve the contact angle to water droplets, endowing nSiO<sub>2</sub> with a better ability to restrain water–salt activity. Our study provides an alternative idea for solving salt damage in murals, and promotes the application of SiO<sub>2</sub> materials in heritage conservation.

**Keywords:** superhydrophobic SiO<sub>2</sub>; mural ground layer; water–salt activity; reinforcement property



**Citation:** Xia, Q.; Dong, W. Research on the Reinforcement and Inhibition of Water–Salt Activity in Mural Ground Layers by Superhydrophobic SiO<sub>2</sub> Particles. *Crystals* **2023**, *13*, 1522. <https://doi.org/10.3390/cryst13101522>

Academic Editor: Carlos Rodriguez-Navarro

Received: 27 August 2023

Revised: 17 October 2023

Accepted: 18 October 2023

Published: 20 October 2023



**Copyright:** © 2023 by the authors. Licensee MDPI, Basel, Switzerland. This article is an open access article distributed under the terms and conditions of the Creative Commons Attribution (CC BY) license (<https://creativecommons.org/licenses/by/4.0/>).

## 1. Introduction

Ancient murals are considered to be the most important cultural relics in human history, and, today, they have valuable and positive influences on the fields of art, history and science. However, ancient murals have suffered from various forms of deterioration, which result from natural environmental factors and human activity [1–3]. Among them, salt damage is one of the most destructive forms of deterioration of ancient murals, and the fundamental reason for the recurrence of salt damage is the water–salt activity inside mural structural materials [4,5]. The main minerals in the ground layer of ancient murals, such as the Mogao Grottoes murals, are quartz, dolomite, calcite, feldspar, illite, chlorite and smectite, and the internal water and salt migrations are unavoidable and active. When the relative humidity of the storage environment changes, the ground layer absorbs moisture or dehumidifies accordingly, causing the water and soluble salts to migrate around the murals. Because of the continuous salt migration, crystallization and accumulation over time, salt damage to ancient murals occur easily, which brings huge challenges for the conservation of murals [5,6].

Salt damage to murals is a common phenomenon around the world. Jin's group [7] conducted simulation experiments on the salt damage of the Dunhuang Mogao Grottoes

murals caused by soluble salts, and characterized the migration and distribution of soluble salts in murals systematically. They found that  $\text{Na}_2\text{SO}_4$  and  $\text{NaCl}$  are the dominant soluble salts with strong abilities of penetration, migration and crystallization in murals. Many works [8–11] have verified that water enters the mural materials mainly through the gaseous state and liquid state, and the water activity was the main driving force for soluble salt transportation. Jia's team studied [1] the capillary behaviors of water and salt in murals, pointing out that the salt was more likely to accumulate in the area of the capillary front after soluble salt capillary migrations. Given that wettability is closely related to the capillary phenomenon, the small contact angle of murals to water droplets always suggests strong capillary activities of water and soluble salt, especially in the ground layer. Generally, the above studies demonstrate that the hydrophilicity of the structural layers of murals are the important factor in salt damage, which should be considered in practical mural conservations.

In order to protect ancient murals, various protection materials have been developed, which could be divided into two kinds: organic protection materials and inorganic protection materials. Since the 1960s, Italian cultural preservation researchers [12–14] have utilized polymer materials such as acrylic polymers and epoxy resins to reinforce and repair ancient frescoes from the Renaissance. Su's team [15,16] compared the comprehensive protection effects of five kinds of polymer resin materials on murals, and found that the reinforcement performance of silicone–acrylic resin copolymers was the best. In comparisons of polymer protection materials, inorganic protection materials exhibit better compatibility, weather resistance and air permeability, and the relevant research has become one of the new hotspots in mural conservations. The P. Baglioni team [17] studied the reinforcement mechanism of  $\text{Ca}(\text{OH})_2$  and  $\text{Ba}(\text{OH})_2$  on murals in detail, and the carbonation process of as-used materials was the key to the reinforcement of mural structure layers. Li's group [18,19] proposed a new strategy of using graphene to assist the nucleation and growth of  $\text{Ca}(\text{OH})_2$ , which was successfully applied to several murals of the Tang tombs. However, current mural protection materials mainly focus on the reinforcement performance of murals, and less in-depth research has been reported on how to improve the wettability characteristics inside murals to overcome salt damage, especially preparing superhydrophobic interfaces to prevent the water–salt activity.

$\text{SiO}_2$  is a common material for the protection of cultural relics [20–25], owing to its excellent compatibility, durability and weather resistance. Wang et al. [20] prepared hydrophobic coatings on ancient bricks via a nano- $\text{SiO}_2/\text{TiO}_2$  hybrid fluorinated B-72 composite, effectively avoiding the adhesion of air pollutants. Zhu et al. [22] studied nanosized  $\text{ZnO}/\text{SiO}_2$ -based amphiphobic coatings for stone heritage protection, and the hydrophobicity was almost unchanged after 300 h of UV irradiation, indicating the composite possessed a good UV absorption capacity and durability. Although most cases of  $\text{SiO}_2$  application in heritage protection have involved the conservation of ancient bricks and stones [20,22,26,27], there are very few pieces of research related to murals. Herein, we chose superhydrophobic  $\text{SiO}_2$  to improve the wettability and reinforcement properties of mural ground layers. With the help of many characterization techniques, the diffusion ability of  $\text{SiO}_2$  with different sizes in the ground layer was studied. Meanwhile, the restraining effect on water–salt migrations and the mechanical reinforcement effect of  $\text{SiO}_2$  on the ground layer were evaluated systematically. This work verifies the positive effect of superhydrophobic  $\text{SiO}_2$  on the ground layer of murals, and the idea of wettability modifications will be promotive and beneficial for developing novel heritage protection materials for other culture relics.

## 2. Materials and Methods

### 2.1. Experimental Materials

Two kinds of superhydrophobic  $\text{SiO}_2$  particles with particle sizes of 300 nm and 20 nm were purchased from Sinopharm Chemical Reagent Co., Ltd., in Shanghai, China. Specifically, the superhydrophobic  $\text{SiO}_2$  particles with a diameter of 300 nm were labeled as

mSiO<sub>2</sub>, and the superhydrophobic SiO<sub>2</sub> particles with a diameter of 20 nm were labeled as nSiO<sub>2</sub>. Ethanol, NaCl and Na<sub>2</sub>SO<sub>4</sub> were purchased from Macklin Biochemical Technology Co., Ltd., in Shanghai, China. Moreover, the substrate resource was collected at the Xi'an Tianma Road site, and the simulated samples of mural ground layers were prepared based on the material ratio of the ancient mural ground [6,28]. Briefly, the collected soil samples were processed into a granular particle state by rolling and crushing, and the substrate particles were passed through a 100-mesh sieve to obtain the screened substrate samples. Subsequently, the screened substrate samples were pressed into the ground layers with a diameter of 50 mm and a height of 20 mm, and then dried at 40 °C.

### 2.2. SiO<sub>2</sub> Infiltration Treatments on the Mural Ground Layers

Two g/L superhydrophobic SiO<sub>2</sub> ethanol dispersion systems were utilized to brush the mural ground layer samples, until the samples could no longer absorb. Subsequently, the treated ground layer samples were dried in the shade indoors.

### 2.3. Characterization and Evaluation Methods

The microstructures of the superhydrophobic SiO<sub>2</sub> and mural ground layer samples were studied by laser scanning confocal microscopy (CLSM, OLS3000, Olympus Corporation, Tokyo, Japan), and scanning electron microscopy (SEM, Stemi 508, ZEISS, Hebron, KY, USA) equipped with an energy dispersive spectrum (EDS). The phase compositions of the samples were characterized by X-ray diffraction (XRD, Rigaku D/max-γB, Tokyo, Japan) with Cu K α (λ = 0.15406 nm) radiation, and the scanning rate was 2°/min. The Fourier transform infrared spectrum of the sample was studied by FTIR spectrometer (FTS165, Bio-Rad, Berkeley, CA, USA). The wetting characteristics of the sample surface were evaluated by contact angle measurement (JC 2000D5, Zhongchen, China). Furthermore, the mechanical strength of the ground layer samples before and after reinforcement was studied by a scratching tester (WS-2005, Wotuo, China), and the color appearance changes of the ground layer samples before and after the infiltration treatment were detected with a colorimeter (VS450, X-rite, Granville, OH, USA). The water–salt behavior inside the mural ground layer samples was evaluated by the soluble salt aqueous solution penetration test.

### 2.4. Dry–Wet Cycle Experiments

Firstly, the ground layer samples were placed on filter papers, which were fully moistened with a 1 g/L NaCl or Na<sub>2</sub>SO<sub>4</sub> solution for 4 h, and the soluble salt could diffuse from the bottom to the top of the ground layer samples via capillary water activity. After the diffusion process, the samples were dried at 40 °C for 12 h. Then, the samples were post-treated with dry (RH = 25%, 2 h) and wet (RH = 95%, 2 h) cycles at 15 °C. After three cycles, the soluble salt distributions from the bottom and the top of ground layer samples were analyzed by EDS. The ground layer samples contained the initial ground layer substrate, the ground layer substrate treated with mSiO<sub>2</sub> (on the top surface), and the ground layer substrate treated with nSiO<sub>2</sub> (on the top surface).

## 3. Results and Discussions

### 3.1. Superhydrophobic SiO<sub>2</sub>

Figure 1a,b demonstrates the microscopic morphology of the two kinds of superhydrophobic SiO<sub>2</sub>, and it can be seen that both the nSiO<sub>2</sub> and mSiO<sub>2</sub> exhibited typical spherical structures. The diameter of mSiO<sub>2</sub> was about 300 nm, and most particles were relatively uniform. By contrast, the diameter of nSiO<sub>2</sub> was about 20 nm, and a certain degree of aggregation occurred, which is most likely related to the particle size. The smaller size endows nSiO<sub>2</sub> with a larger specific surface area and therefore a higher specific surface energy, and so nSiO<sub>2</sub> agglomerates more easily in thermodynamics than mSiO<sub>2</sub>. Figure 1c displays the XRD patterns of mSiO<sub>2</sub> and nSiO<sub>2</sub>. Evidently, there are no obvious characteristic diffraction peaks in the XRD patterns, implying that both of them exist in an amorphous state [29,30]. Moreover, an obvious bulge appears in the range of 20~30° in the patterns,

which corresponds to the strongest characteristic diffraction peaks of crystalline  $\text{SiO}_2$ . The bulge peak for the amorphous phase of  $\text{mSiO}_2$  is slightly narrower than that of  $\text{nSiO}_2$ , indicating that the short-range arrangement increases as the size of superhydrophobic  $\text{SiO}_2$  increases.

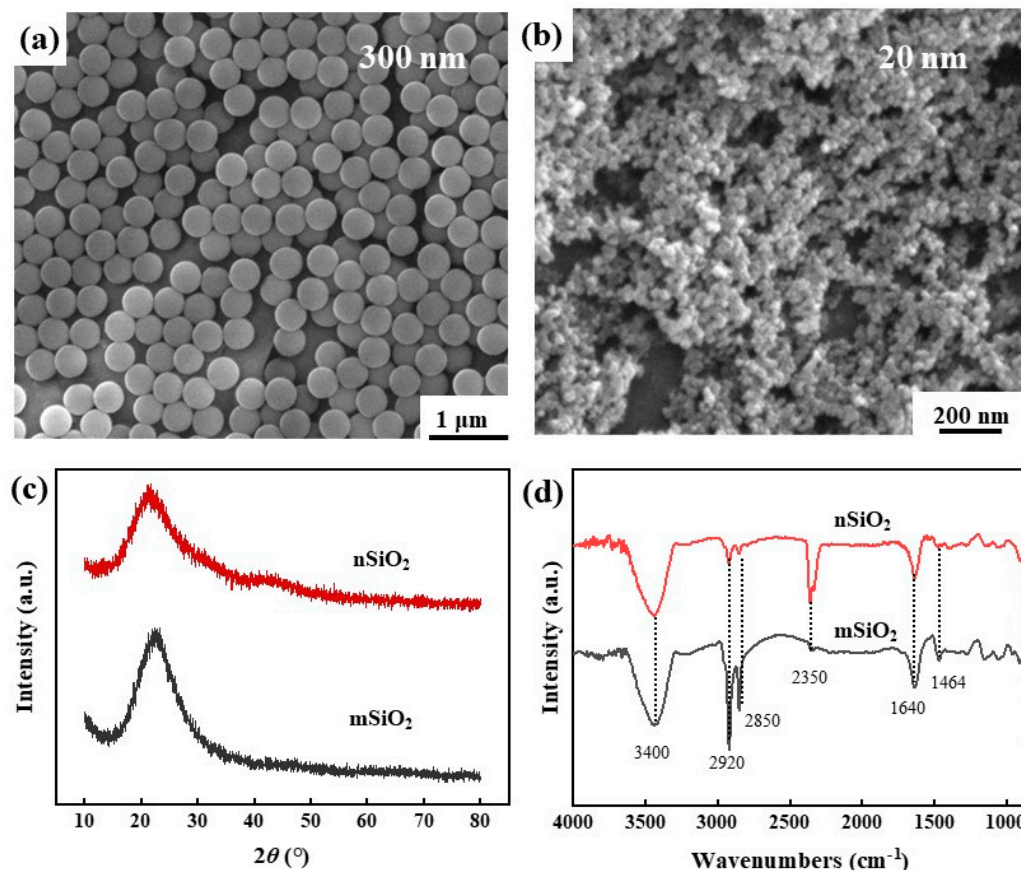


**Figure 1.** SEM morphologies (a,b), XRD patterns (c) and FTIR results (d) of  $\text{mSiO}_2$  and  $\text{nSiO}_2$ .

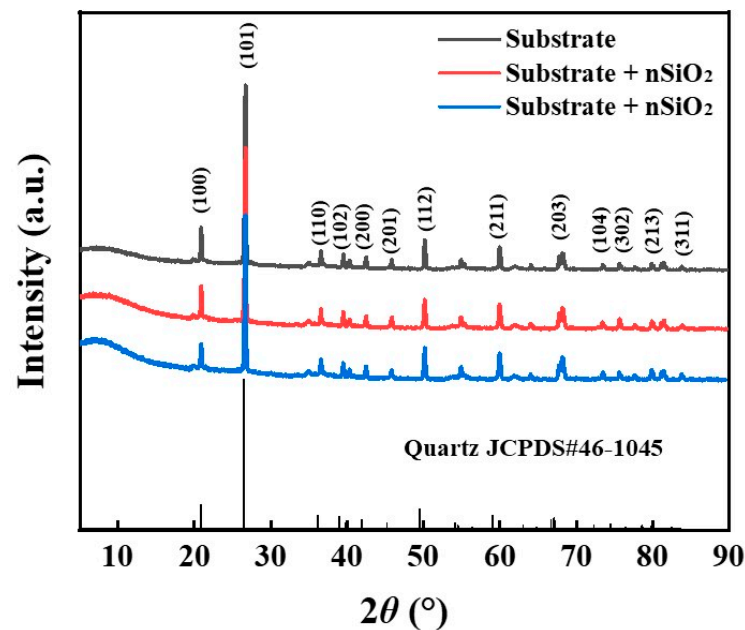
Figure 1d demonstrates the IR analysis results of the  $\text{mSiO}_2$  and  $\text{nSiO}_2$ , and there are many peaks at the positions of  $3400\text{ cm}^{-1}$ ,  $2920\text{ cm}^{-1}$ ,  $2850\text{ cm}^{-1}$ ,  $2350\text{ cm}^{-1}$ ,  $1640\text{ cm}^{-1}$  and  $1464\text{ cm}^{-1}$ . Among them, the peak at  $3400\text{ cm}^{-1}$  corresponds to the stretching vibration of  $-\text{OH}$  on the  $\text{SiO}_2$  surface [31], and the peak at  $2350\text{ cm}^{-1}$  is related to the stretching vibration of the  $\text{C}=\text{O}$  bond [32], indicating that  $\text{CO}_2$  in the air is adsorbed on the  $\text{SiO}_2$  surface. Although the two kinds of  $\text{SiO}_2$  materials have the superhydrophobic property, the absorption peak of  $\text{H}_2\text{O}$  molecules ( $1640\text{ cm}^{-1}$ ) was still detected on the surface. Meanwhile, the peak at  $2920\text{ cm}^{-1}$  matches with the stretching vibration of  $-\text{CH}_3$  or  $\text{C}-\text{H}$  bonds, the peak at  $2850\text{ cm}^{-1}$  is assigned to the stretching vibration of  $-\text{CH}_2-\text{CH}_3$  bonds, and the peak at  $1464\text{ cm}^{-1}$  is related to the in-plane bending vibration of  $-\text{CH}_3$  [33,34]. Namely, abundant hydrophobic groups exist on the  $\text{SiO}_2$  surface, which is the main reason for the transformation of the  $\text{SiO}_2$  surface from having a normal hydrophilic property to a hydrophobic property. Table 1 illustrates the EDS results of the  $\text{mSiO}_2$  and  $\text{nSiO}_2$ . Evidently, the two kinds of superhydrophobic  $\text{SiO}_2$  are mainly composed of Si, O and C. The C-source might be the hydrophobic functional groups and contaminating carbon. The above results indicate that  $\text{mSiO}_2$  and  $\text{nSiO}_2$  possess similar compositions and surface characteristics, except for the difference in particle size.

**Table 1.** The EDS results for mSiO<sub>2</sub> and nSiO<sub>2</sub>.

Element	Si (at.%)	O (at.%)	C (at.%)
mSiO <sub>2</sub>	24	55	17
nSiO <sub>2</sub>	22	49	23

### 3.2. Comprehensive Characterizations

Figure 2 presents the XRD results of the ground layer substrate before and after the superhydrophobic SiO<sub>2</sub> infiltration treatment. Strong diffraction peaks are observed at 20.8°, 26.6°, 36.5°, 39.4° and 50.1° in the XRD pattern, corresponding to the characteristic peaks of quartz-SiO<sub>2</sub> (JCPDS#46-1045) [35]. The initial ground layer substrate (substrate), the ground layer substrate with nSiO<sub>2</sub> (substrate + nSiO<sub>2</sub>) and the ground layer substrate with mSiO<sub>2</sub> (substrate + mSiO<sub>2</sub>) present similar characteristics in the XRD patterns, which might result from the fact that both nSiO<sub>2</sub> and mSiO<sub>2</sub> with amorphous states struggle to bring apparent change to the quartz-SiO<sub>2</sub> in XRD patterns. Table 2 shows the EDS results of the ground layer substrates, and the main element compositions are Si, O, Al, C, Fe, etc. Given that the samples were prepared from ancient mural ground layer substrates [28], the main phase of the earthen materials is quartz-SiO<sub>2</sub>, and other components are very small. To a certain extent, it could be obtained that both mSiO<sub>2</sub> and nSiO<sub>2</sub> are compatible with mural ground layer substrates.

**Figure 2.** XRD results of the ground layer substrate before and after superhydrophobic SiO<sub>2</sub> infiltration treatment at 5~90°.**Table 2.** The EDS results of mSiO<sub>2</sub> and nSiO<sub>2</sub>.

Element	Si (at.%)	O (at.%)	Al (at.%)	C (at.%)	Fe (at.%)	Ca (at.%)
Substrate	18.76	50.93	5.55	23.38	1.03	0.35
Substrate + mSiO <sub>2</sub>	20.26	47.92	4.67	25.37	1.44	0.34
Substrate + nSiO <sub>2</sub>	23.38	52.09	6.99	17.15	0.39	-

The CLSM and SEM morphologies of the ground layer substrate before and after the SiO<sub>2</sub> infiltration treatment are shown in Figure 3. Before SiO<sub>2</sub> infiltration treatment, the surface of the initial ground layer substrate was uneven and choppy, and the surface roughness was 42.3 μm. After the SiO<sub>2</sub> infiltration treatment, the undulation of the ground

layer substrate gradually decreased, and the surface roughness reduced accordingly. In particular, the surface roughness of the ground layer substrate after the nSiO<sub>2</sub> treatment was 28.8 μm, while that of the substrate with mSiO<sub>2</sub> treatment was 35.1 μm. In addition, the SEM results illustrate the microstructural changes of the ground layer substrate before and after treatment. The initial ground layer contains many irregular earthen material particles, and possesses numerous gaps between adjacent particles. After the SiO<sub>2</sub> treatment, the substrate surface was covered with nSiO<sub>2</sub> (Figure 3(b2)) or mSiO<sub>2</sub> (Figure 3(c2)), and the original uneven area was filled with nSiO<sub>2</sub> or mSiO<sub>2</sub>, which led to the decline of the surface roughness. Because the size of mSiO<sub>2</sub> is larger than that of nSiO<sub>2</sub>, the modification effect on the substrate surface was much stronger, so mSiO<sub>2</sub> reduces the roughness of the ground layer surface more than nSiO<sub>2</sub>. Figure 4 shows other SEM morphologies of the ground layer substrates with mSiO<sub>2</sub> and nSiO<sub>2</sub>. Both substrates had lots of holes and crays, which could be channels for inward infiltration of superhydrophobic SiO<sub>2</sub> from the surface to the interior. Additionally, there were some exposed parts at the substrate surface with mSiO<sub>2</sub>, suggesting that the expanding ability of mSiO<sub>2</sub> is not as good as that of nSiO<sub>2</sub>. This might be related to the size of the SiO<sub>2</sub>, and the smaller size enables nSiO<sub>2</sub> to spread further than mSiO<sub>2</sub>.

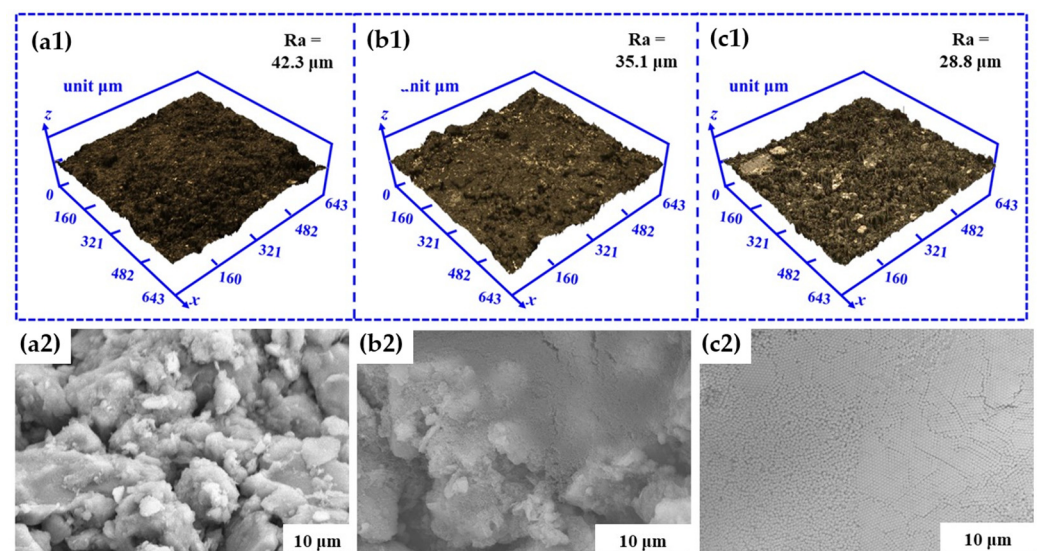


**Figure 3.** The CLSM and SEM morphologies of the ground layer substrate before and after SiO<sub>2</sub> infiltration treatment: (a1,a2) the initial ground layer substrate, (b1,b2) the ground layer substrate treated with nSiO<sub>2</sub>, (c1,c2) the ground layer substrate treated with mSiO<sub>2</sub>.

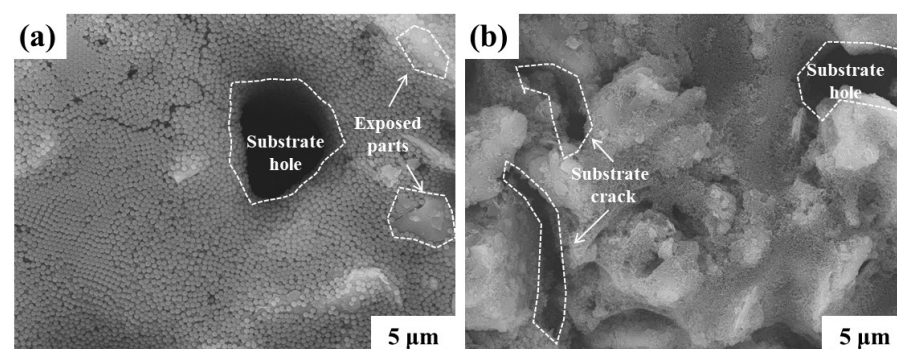


**Figure 4.** The SEM morphologies at other locations of the ground layer substrate with the SiO<sub>2</sub> infiltration treatment: the substrate treated with mSiO<sub>2</sub> (a); the substrate treated with mSiO<sub>2</sub> (b).

The mechanical properties of the ground layer substrate before and after the SiO<sub>2</sub> infiltration treatment were tested by the scratching method, as shown in Figure 5a. When

the same pressure is applied, the shift distances of the indenter in the substrate are positively correlated with the mechanical strength of the ground layer substrate. The shift distances of the indenter in the initial ground layer substrate, the ground layer substrate with nSiO<sub>2</sub>, and the ground layer substrate with mSiO<sub>2</sub> were about 1800 μm, 1200 μm and 700 μm, respectively. Since the substrate samples were easily broken and had poor toughness, the probe position of the scratch meter presents discontinuous features. Even so, the results prove that the SiO<sub>2</sub> infiltration treatment can improve the mechanical properties of the ground layer, and the reinforcement effect of mSiO<sub>2</sub> is better than that of nSiO<sub>2</sub>, which is related to their particle size.

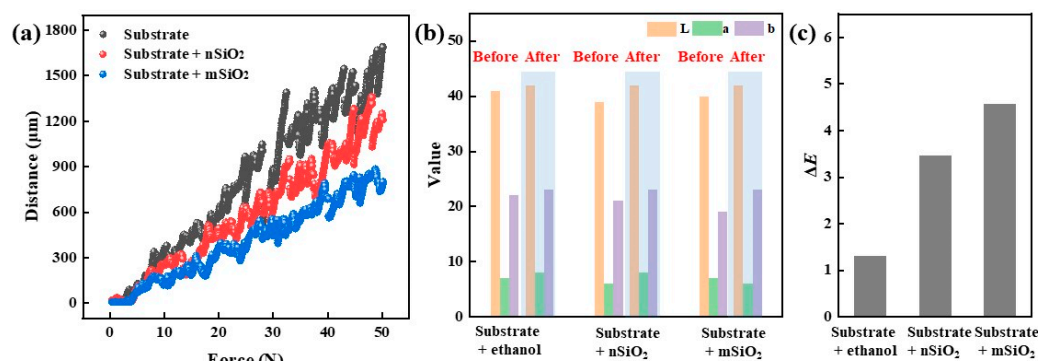
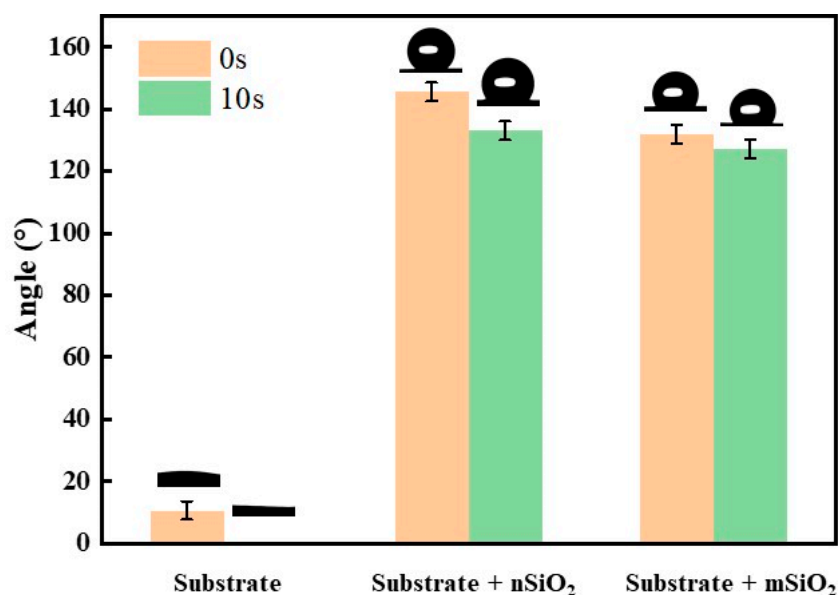


**Figure 5.** Scratching tests (a) and chromaticity value changes (b,c) of the ground layer substrates before and after SiO<sub>2</sub> infiltration treatment.

Furthermore, color change is an important indicator to evaluate whether new materials are suitable for cultural relic protection, and the color difference results of the ground layer before and after the SiO<sub>2</sub> infiltration treatment were studied by the L\*a\*b color space method (Figure 5b,c). For eliminating the disturbances of ethanol on the appearance, a pure ethanol-infiltrated ground layer substrate was employed as the control group. From the L\*a\*b results, it could be seen that the color change values ( $\Delta E$ ) of the ground layer substrates with pure ethanol, nSiO<sub>2</sub> and mSiO<sub>2</sub> were 1.73, 3.46 and 4.58, respectively. Generally, the color difference between mSiO<sub>2</sub> and nSiO<sub>2</sub> is related to the particle size, and the integrated color change values are lower than 5. Owing to the appearance of ground layer substrates changing extremely slightly, it is clearly proved that both nSiO<sub>2</sub> and mSiO<sub>2</sub> are suitable for the protection of ancient murals.

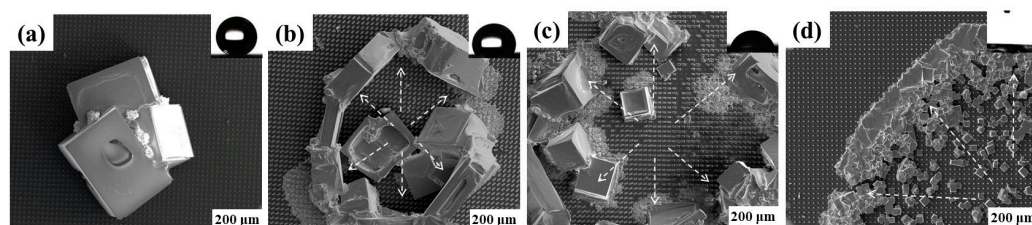
### 3.3. Wettability and Water–Salt Behavior Analysis

Figure 6 demonstrates the contact angle of NaCl aqueous droplets on the surface of the ground layer before and after the infiltration treatment. Being mainly composed of quartz-SiO<sub>2</sub>, the initial ground layer had typical hydrophilic features. When the NaCl aqueous droplet landed on the surface of the initial ground layer substrate, the contact angle of the water droplet was 10.63°. Then, the aqueous droplet completely penetrated into the ground layer substrate for 10 s, and thereby the contact angle dropped to 0°. After being treated with mSiO<sub>2</sub> and nSiO<sub>2</sub>, the wettability of the ground layer substrate surface changed from hydrophilic to hydrophobic. The contact angle of the ground layer substrate with nSiO<sub>2</sub> was 145.5° when the NaCl aqueous droplet first falls on the surface, and the contact angle decreased and stabilized to 133° after 10 s. In contrast, the contact angle of the ground layer substrate with mSiO<sub>2</sub> was 132° when the NaCl aqueous droplet first falls on the surface, and the contact angle decreased slightly to 127° after 10 s. In terms of the wettability modification, the ability of nSiO<sub>2</sub> is slightly higher than that of mSiO<sub>2</sub>, which might be associated with their coverage area on substrates, as presented in Figure 4. Consequently, both nSiO<sub>2</sub> and mSiO<sub>2</sub> can successfully reverse the wettability of the ground layer substrate surface from hydrophilic to hydrophobic.



**Figure 6.** The contact angles of NaCl aqueous droplets for 0 s and 10 s on the surface of the ground layer substrates before and after SiO<sub>2</sub> infiltration treatment.

In order to study the relationship between the surface wettability and the crystallization behavior of soluble salts, we used SEM to observe how the NaCl aqueous droplets crystallized on the four kinds of surfaces (superhydrophobic, hydrophobic, hydrophilic, and superhydrophilic). Figure 7 shows that as the contact angles of the NaCl aqueous droplets decreased, the crystallization area of the NaCl increased, while the size of the NaCl crystals became smaller. Except for the NaCl crystallization at the superhydrophobic interface (Figure 7a), all the other SEM images demonstrate the characteristic of NaCl crystallization spreading from the center along the radius, and this phenomenon is positively related to the contact angle. In other words, NaCl crystallization occurs first at the terminal sites of the NaCl aqueous droplets, and the wettability of the surface promotes the droplets spreading farther, which leads to the NaCl crystallization area becoming larger. Therefore, it could be proved that the superhydrophobic ability of the surface is beneficial to suppressing the activity of water–salt migrations. Meanwhile, the modification of the mural ground layer substrate wettability would be an effective method for inhibiting the damage caused by soluble salts.



**Figure 7.** NaCl crystallization behaviors on surfaces with different wetting characteristics: superhydrophobic (a), hydrophobic (b), hydrophilic (c), superhydrophilic (d).

The water–salt behaviors on the surface and inside of the ground layers were studied with a diffusion experiment of saturated NaCl solution, and the surface crystal morphology of the NaCl on the ground layer substrates were observed (Figure 8). It could be seen that NaCl crystallization appears on the surface of all ground layer substrates, but the NaCl crystals on the initial ground layer were significantly fewer and smaller than those of the ground layers with nSiO<sub>2</sub> and mSiO<sub>2</sub>. Due to the hydrophilic property of the initial substrate, NaCl droplets are more likely to enter the substrate deeply from the surface, and

therefore the number of NaCl crystals is relatively greater in the interior of the substrate. In comparison, more NaCl crystals on the surface of the substrates treated with  $m\text{SiO}_2$  and  $n\text{SiO}_2$  reveal that the amount of NaCl entering the interior of the ground layer substrates declines. Figure 9 illustrates the EDS mapping results of NaCl crystallization on the ground layer with  $n\text{SiO}_2$ . Obviously, the block-shaped crystals are mainly composed of Na and Cl elements, and thus the hydrophobic feature can promote NaCl precipitating from the aqueous solution on the ground layer surface. Combined with the NaCl crystallization phenomenon in Figure 7, it is confirmed that the changes in the surface wettability of the ground layer substrate can efficiently affect the soluble salt crystallization behavior.

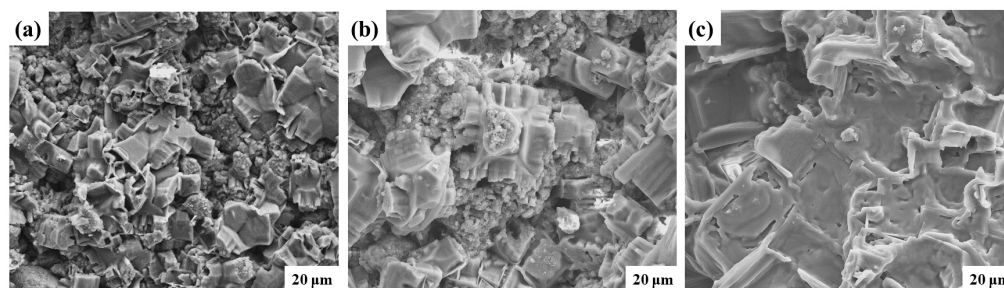


**Figure 8.** NaCl crystallization morphology on the surface of the initial ground layer substrate (a), the ground layer substrate after  $n\text{SiO}_2$  infiltration treatment (b), the ground layer substrate after  $m\text{SiO}_2$  infiltration treatment (c).

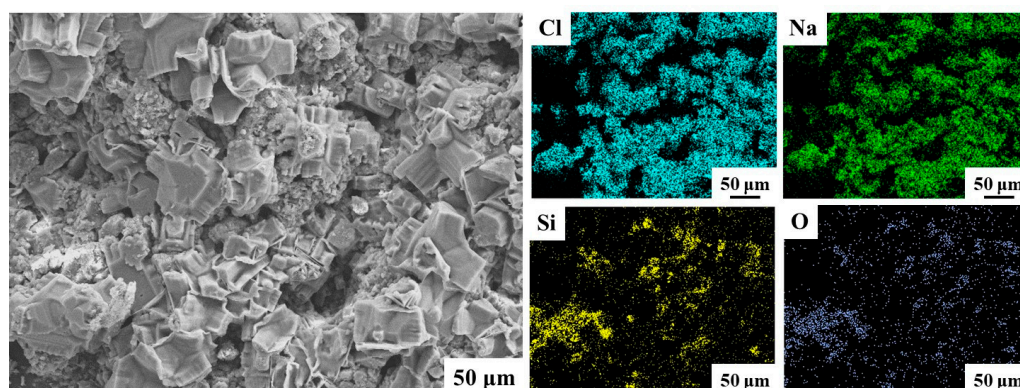


**Figure 9.** The SEM morphology and EDS mapping analysis of NaCl crystallization on the surface of the ground layer substrate after  $n\text{SiO}_2$  infiltration treatment.

In order to study the water–salt behavior inside the ground layers, the tops of the ground layer substrates were carefully removed to expose the inner interfaces of the ground layers at a depth of 1 cm, and EDS analysis was employed to study the content of Na and Cl elements inside the ground layers (Figure 10). Moreover, the other elements in the EDS results were Al, Fe, Ca, Si, O and C. It was found that the content of the Na element and Cl element at a depth of 1 cm in the initial ground layer was 5.3 wt.% and 3.3 wt.%, respectively; After the  $m\text{SiO}_2$  treatment, the Na element and Cl element content in the ground layer was 3.2 wt.% and 1.2 wt.% respectively. After the  $n\text{SiO}_2$  treatment, the Na element and Cl element content was 3.2 wt.% and 1.2 wt.%, respectively. Calculated by the change in Cl element, the inhibition rate of  $n\text{SiO}_2$  and  $m\text{SiO}_2$  to the water–salt activity inside the ground layer substrate was 0.36 and 0.24, which indicates that the water–salt activity inside the ground layer substrate was restrained after the superhydrophobic  $\text{SiO}_2$  treatment, and  $n\text{SiO}_2$  has a relatively greater ability than  $m\text{SiO}_2$ .

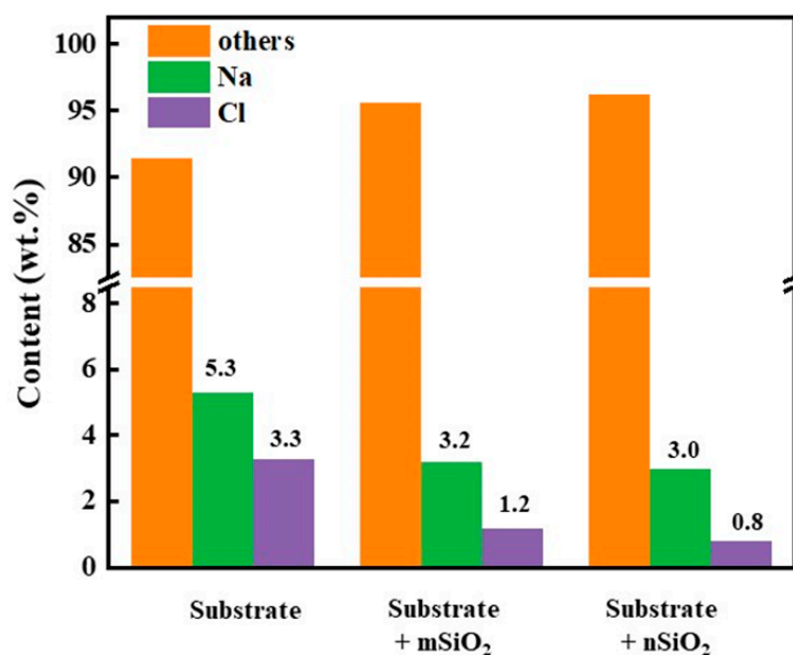


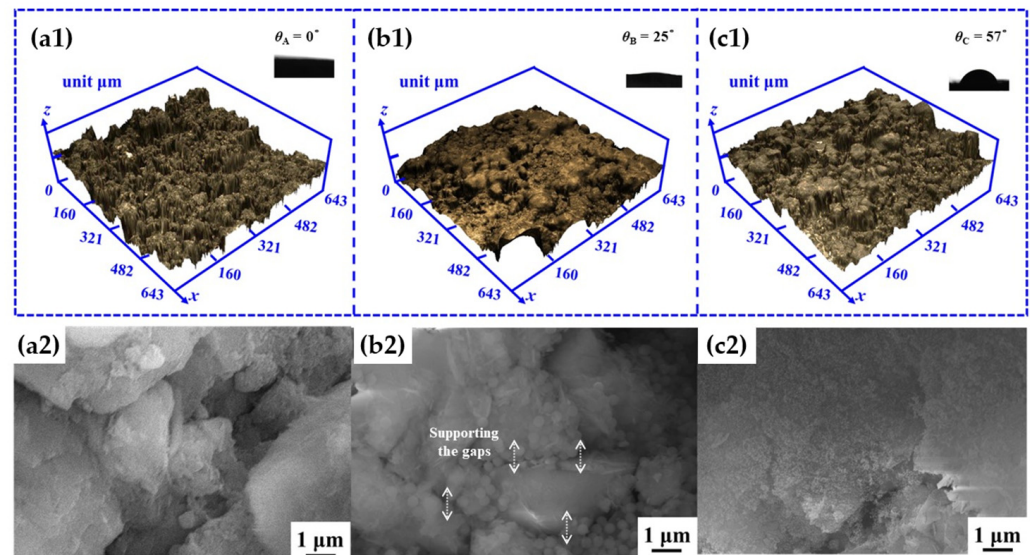
**Figure 10.** The EDS contents of Na and Cl elements at 1 cm inside the ground layer substrate before and after SiO<sub>2</sub> treatments.

### 3.4. Mechanism Analysis

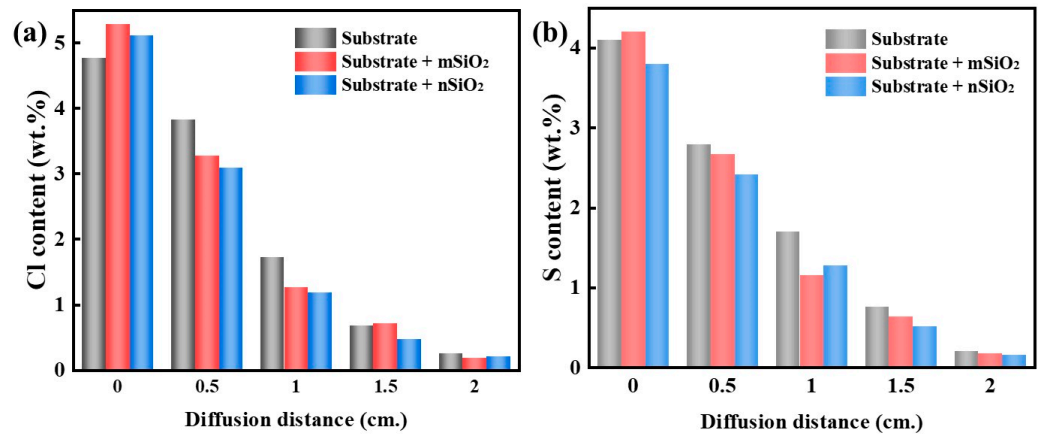
The above test results conclude that both mSiO<sub>2</sub> and nSiO<sub>2</sub> can enhance the mechanical properties and inhibit water–salt activity of the ground layer substrate. Specially, mSiO<sub>2</sub> presents the better effect on mechanical properties, while nSiO<sub>2</sub> exhibits the better performance in inhibiting the water–salt activity inside the ground layer. In order to discover the internal reasons for this difference, we systematically studied the state of the ground layer substrates at a depth of 5 mm, as displayed in Figure 11. At the depth of 5 mm, the contact angle of the initial ground layer substrate was 0° ( $\theta_A$ ), while the contact angles of the ground layer substrates with mSiO<sub>2</sub> and nSiO<sub>2</sub> were 25° ( $\theta_B$ ) and 57° ( $\theta_C$ ), respectively. The SEM results disclose that both mSiO<sub>2</sub> and nSiO<sub>2</sub> diffuse to the depth of 5 mm in the ground layer, but the amount of mSiO<sub>2</sub> is significantly less than that of nSiO<sub>2</sub>, revealing that the smaller particle size facilitates the nSiO<sub>2</sub> in penetrating the inner substrates and suppressing droplet expansion. Hence, nSiO<sub>2</sub> particles possess the better effect of inhibiting water–salt activity in the inner substrates compared to mSiO<sub>2</sub>. Furthermore, the internal mSiO<sub>2</sub> existing in the gaps between substrate particles can effectively support the inside of the substrate, but it is difficult for the internal nSiO<sub>2</sub> with a smaller particle size to play a significant role in supporting the particle gaps in earthen materials, resulting in mSiO<sub>2</sub> possessing the better ability in improving mechanical properties compared to nSiO<sub>2</sub>.

Figure 12 presents the element distributions from the bottom to the top of the ground layer substrates after the soluble salt diffusion (1 g/L) and post-RH cycling experiments, for evaluating NaCl or Na<sub>2</sub>SO<sub>4</sub> behaviors during wet/dry humidity cycles. The Cl and S contents are used to represent the content of NaCl and Na<sub>2</sub>SO<sub>4</sub>, respectively. Overall, the internal salt content of the SiO<sub>2</sub>-treated substrate was lower than that of the initial ground layer substrate, which suggests that SiO<sub>2</sub> is conducive to inhibiting water–salt activities inside the substrate. In addition, the distribution phenomena of NaCl inside the ground substrate are basically the same as that of Na<sub>2</sub>SO<sub>4</sub>. As the diffusion distance increases from the bottom to the top, the soluble salt content gradually decreases. This might be because the more SiO<sub>2</sub> on the top of the ground layer substrate, the greater the impact on the capillary water–salt activity. Furthermore, there was no large-scale aggregation of soluble salts observed inside the ground layer substrates, and the distribution of soluble salts was continuous, which indicates that SiO<sub>2</sub> treatment would not act as a barrier to prevent the

migration of the salt to the surface. This can be explained by the changes in contact angle in the internal substrate: because the superhydrophobic  $\text{SiO}_2$  content decreases continuously from the top to the bottom, and therefore the contact angle increases continuously and gradually from the bottom to the top, the diffusion resistance from  $\text{SiO}_2$  is also continuous. Therefore, it could be proved that  $\text{SiO}_2$  treatment does not cause extra harm to the ground layer substrate, and superhydrophobic  $\text{SiO}_2$  possesses a better compatibility than organic protective materials.



**Figure 11.** The CLSM, SEM and contact angle results of the ground-strand layer sample at a depth of 5 mm: the initial ground layer substrate (a1,a2), the ground layer substrate treated with mSiO<sub>2</sub> (b1,b2), the ground layer substrate treated with nSiO<sub>2</sub> (c1,c2).



**Figure 12.** The Cl and S element distributions from the bottom to top of ground layer substrates after the soluble salt diffusion and post-RH cycling experiments: NaCl (a), Na<sub>2</sub>SO<sub>4</sub> (b).

Figure 13 reveals more clearly the two kinds of effect mechanisms of the superhydrophobic  $\text{SiO}_2$  on the ground layer substrates. Superhydrophobic  $\text{SiO}_2$  enters the inner substrate through channels such as pores and cracks. On the one hand,  $\text{SiO}_2$  can support the cracks between the internal gaps of substrate particles, and on the other hand, the wettability of the inner substrate changes, thereby inhibiting water–salt activities in the channels within the substrate. Certainly, the size of the  $\text{SiO}_2$  particles explains their different roles in the mechanical supporting effect (Figure 13a) and restraining capillary water–salt activity (Figure 13b). The bigger particle (mSiO<sub>2</sub>) is relatively close to the scale of the gaps inside the substrate, so mSiO<sub>2</sub> can perform a better mechanical supporting effect than nSiO<sub>2</sub>. In

addition, nSiO<sub>2</sub> can penetrate deeper than mSiO<sub>2</sub> through the channels inside the substrate, and so the contact angle of water droplets to the substrate with nSiO<sub>2</sub> is higher than that with mSiO<sub>2</sub>. From the refs [1,11,27], the water–salt activity inside the substrate can be regarded as a capillary phenomenon to some extent (Figure 13b), which is very relevant to the contact angle. When the contact angle of the interior substrate becomes higher, the capillary water–salt behavior is affected more strongly, and thus nSiO<sub>2</sub> possesses the better ability of restraining the capillary water–salt activity inside the ground layer substrate compared to mSiO<sub>2</sub>.

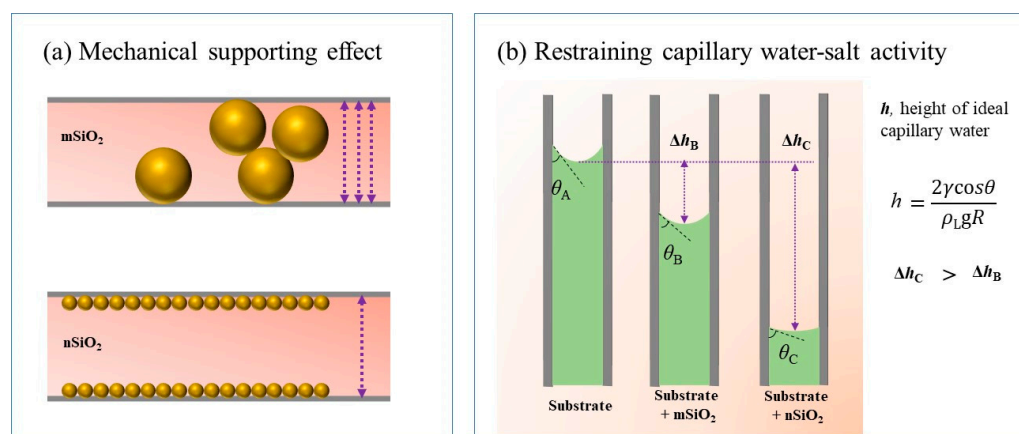


**Figure 13.** Schematic diagrams of the mechanical supporting effect of SiO<sub>2</sub> particles on the ground layer inner gaps (a) and the restraining effect of capillary water–salt activity (b).

#### 4. Conclusions

- (1) We systematically studied the improvement effects of superhydrophobic SiO<sub>2</sub> on the conservation of mural ground layer substrate. Superhydrophobic SiO<sub>2</sub> particles are composed of an amorphous phase and abundant hydrophobic functional groups, and the substrates of mural ground layers mainly consist of quartz-SiO<sub>2</sub>, endowing the superhydrophobic SiO<sub>2</sub> with good compatibility with the substrate. In addition, the superhydrophobic SiO<sub>2</sub> can penetrate into the interior substrate through holes and cracks on the surface, and the appearance of the substrate changes little after SiO<sub>2</sub> infiltration treatments.
- (2) The treatments of superhydrophobic SiO<sub>2</sub> not only effectively modify the wettability of the substrate from hydrophilicity to hydrophobicity, but also increase the contact angle of water droplets in the interior substrate. By supporting the internal gaps in substrates, the superhydrophobic SiO<sub>2</sub> can enhance the strength of the substrates, and the reinforcement effect is positively correlated to the size of the SiO<sub>2</sub> particles. Moreover, the superhydrophobic SiO<sub>2</sub> can affect the capillary water–salt behavior inside the substrate and prevent salt damage. Smaller SiO<sub>2</sub> particles penetrate the substrate deeper and obtain a higher contact angle to water droplets, and thereby nSiO<sub>2</sub> possesses a better restraining effect on the water–salt activity than mSiO<sub>2</sub>.
- (3) This work verifies the availability of modifying the wettability of substrate samples by superhydrophobic SiO<sub>2</sub> treatment, and that salt damage of mural ground layers can be suppressed without causing excessive aggregations of soluble salts, which provides a new insight for designing effective mural protection materials. In the future, we will focus more attention on developing superhydrophobic SiO<sub>2</sub> materials with a hierarchical structure, which can hold multi-scale effects and express promising prospects in the prevention of salt damage to ancient murals.

**Author Contributions:** Q.X.—conceptualization, methodology, investigation, writing original and reviewing draft, and funding acquisition; W.D.—funding acquisition and supervision. All authors have read and agreed to the published version of the manuscript.

**Funding:** This research is supported by Shaanxi Provincial Natural Science Basic Research Program (2021JQ-093), the Shaanxi Provincial Social Science Fund Project (2023G010), the National Natural Science Foundation of China (52101272), and the Fundamental Research Funds for the Central Universities of Northwestern Polytechnical University (31020200QD004).

**Data Availability Statement:** The data presented in this study are available on request from the author.

**Conflicts of Interest:** The authors declare that they have no known competing financial interest or personal relationships that could have appeared to influence the work reported in this paper.

## References

1. Jia, Q.; Chen, W.; Tong, Y.; Guo, Q. Experimental Study on Capillary Migration of Water and Salt in Wall Painting Plaster A Case Study at Mogao Grottoes, China. *Int. J. Archit. Herit.* **2022**, *16*, 705–716. [[CrossRef](#)]
2. Peng, J.; Yu, K.; Wang, J.; Zhang, Q.; Wang, L.; Fan, P. Mining painted cultural relic patterns based on principal component images selection and image fusion of hyperspectral images. *J. Cult. Herit.* **2019**, *36*, 32–39. [[CrossRef](#)]
3. Li, J.; Zhang, H.; Fan, Z.; He, X.; He, S.; Sun, M.; Ma, Y.; Fang, S.; Zhang, H.; Zhang, B. Investigation of the renewed diseases on murals at Mogao Grottoes. *Herit. Sci.* **2013**, *1*, 31. [[CrossRef](#)]
4. Tarantola, G.; Medri, E.; Splendore, A.; Lo Russo, F.; Matteucci, C.; Minelli, M. Liquid Foam-Ethyl Vinyl Acetate Adhesive Systems for Lining Process of Paintings: Prospects of a User-Friendly, Harmless Alternative to Conventional Products. *Polymers* **2023**, *15*, 1741. [[CrossRef](#)] [[PubMed](#)]
5. He, D.; Wu, F.; Ma, W.; Zhang, Y.; Gu, J.-D.; Duan, Y.; Xu, R.; Feng, H.; Wang, W.; Li, S.-W. Insights into the bacterial and fungal communities and microbiome that causes a microbe outbreak on ancient wall paintings in the Maijishan Grottoes. *Int. Biodeterior. Biodegrad.* **2021**, *163*, 105250. [[CrossRef](#)]
6. Shen, L.; Kirino, F.; Tsukada, A.; Du, X. Material and technical study of the mural paintings at Ta'erliang Village, Inner Mongolia. *Sci. Conserv. Archaeol.* **2019**, *6*, 7–14.
7. Li, F.; Wang, X.; Guo, Q.; Zhang, B.; Pei, Q.; Yang, S. Moisture adsorption mechanism of earthen plaster containing soluble salts in the Mogao Grottoes of China. *Stud. Conserv.* **2019**, *64*, 159–173. [[CrossRef](#)]
8. Li, F.; Liu, H.; Yang, H.; Ayyamperumal, R.; Liu, Y. Influence of water vapor sorption of NaCl-Na<sub>2</sub>SO<sub>4</sub>-containing mural earthen plaster and preliminary deterioration analysis. *Total Environ. Res. Themes* **2023**, *6*, 100040. [[CrossRef](#)]
9. Godts, S.; Hayen, R.; De Clercq, H. Investigating salt decay of stone materials related to the environment, a case study in the St. James church in Liège, Belgium. *Stud. Conserv.* **2017**, *62*, 329–342. [[CrossRef](#)]
10. Zhao, J.; Luo, H.; Huang, X. Migration, Crystallization and Dissolution Changes of Salt Solution with Color Rendering Property in Porous Quartz Materials. *Molecules* **2020**, *25*, 5708. [[CrossRef](#)]
11. He, X.; Li, J.; Tao, L.; Zhang, B.; Fan, Z.; Su, B. Mechanisms of preservation damage: Restoration materials affecting salt distribution and soil expansion in wall paintings of Dunhuang. *Archaeol. Anthropol. Sci.* **2019**, *11*, 5171–5179. [[CrossRef](#)]
12. La Nasa, J.; Orsini, S.; Degano, I.; Rava, A.; Modugno, F.; Colombini, M.P. A chemical study of organic materials in three murals by Keith Haring: A comparison of painting techniques. *Microchem. J.* **2016**, *124*, 940–948. [[CrossRef](#)]
13. Carretti, E.; Dei, L. Physicochemical characterization of acrylic polymeric resins coating porous materials of artistic interest. *Prog. Org. Coat.* **2004**, *49*, 282–289. [[CrossRef](#)]
14. Carretti, E.; Dei, L.; Baglioni, P. Solubilization of acrylic and vinyl polymers in nanocontainer solutions. Application of microemulsions and micelles to cultural heritage conservation. *Langmuir* **2003**, *19*, 7867–7872. [[CrossRef](#)]
15. Bomin, S.; Huabing, Z.; Binjian, Z.; Deqiang, J.; Rui, Z.; Xiang, T. A scientific investigation of five polymeric materials used in the conservation of murals in Dunhuang Mogao Grottoes. *J. Cult. Herit.* **2018**, *31*, 105–111. [[CrossRef](#)]
16. Han, P.; Zhang, H.; Zhang, R.; Tan, X.; Zhao, L.; Liang, Y.; Su, B. Evaluation of the effectiveness and compatibility of nanolime for the consolidation of earthen-based murals at Mogao Grottoes. *J. Cult. Herit.* **2022**, *58*, 266–273. [[CrossRef](#)]
17. Giorgi, R.; Ambrosi, M.; Toccafondi, N.; Baglioni, P. Nanoparticles for cultural heritage conservation: Calcium and barium hydroxide nanoparticles for wall painting consolidation. *Chem. A Eur. J.* **2010**, *16*, 9374–9382. [[CrossRef](#)]
18. Zhu, J.; Li, X.; Zhang, Y.; Wang, J.; Wei, B. Graphene-enhanced nanomaterials for wall painting protection. *Adv. Funct. Mater.* **2018**, *28*, 1803872. [[CrossRef](#)]
19. Zhu, J.; Zhang, P.; Ding, J.; Dong, Y.; Cao, Y.; Dong, W.; Zhao, X.; Li, X.; Camaiti, M. Nano Ca(OH)<sub>2</sub>: A review on synthesis, properties and applications. *J. Cult. Herit.* **2021**, *50*, 25–42. [[CrossRef](#)]
20. Wang, K.; Bu, N.; Zhen, Q.; Liu, J.; Bashir, S. Modified nano-SiO<sub>2</sub>/TiO<sub>2</sub> hybrid fluorinated B-72 as antimicrobial and hydrophobic coatings for the conservation of ancient bricks. *Constr. Build. Mater.* **2023**, *365*, 130090. [[CrossRef](#)]
21. Pino, F.; Fermo, P.; La Russa, M.; Ruffolo, S.; Comite, V.; Baghdachi, J.; Pecchioni, E.; Fratini, F.; Cappelletti, G. Advanced mortar coatings for cultural heritage protection. Durability towards prolonged UV and outdoor exposure. *Environ. Sci. Pollut. Res.* **2017**, *24*, 12608–12617. [[CrossRef](#)] [[PubMed](#)]
22. Yumei, C.; Gang, W.; Pei, S.; Luo, H.; Xichen, Z.; Biao, Z.; Zhu, J. Nanosized ZnO/SiO<sub>2</sub>-Based Amphiphobic Coatings for Stone Heritage Protection. *ACS Appl. Nano Mater.* **2022**, *5*, 18708–18717. [[CrossRef](#)]

23. Crupi, V.; Fazio, B.; Gessini, A.; Kis, Z.; La Russa, M.F.; Majolino, D.; Masciovecchio, C.; Ricca, M.; Rossi, B.; Ruffolo, S.A.; et al. TiO<sub>2</sub>-SiO<sub>2</sub>-PDMS nanocomposite coating with self-cleaning effect for stone material: Finding the optimal amount of TiO<sub>2</sub>. *Constr. Build. Mater.* **2018**, *166*, 464–471. [[CrossRef](#)]
24. Barberio, M.; Veltri, S.; Imbrogno, A.; Stranges, F.; Bonanno, A.; Antici, P. TiO<sub>2</sub> and SiO<sub>2</sub> nanoparticles film for cultural heritage: Conservation and consolidation of ceramic artifacts. *Surf. Coat. Technol.* **2015**, *271*, 174–180. [[CrossRef](#)]
25. Zornoza-Indart, A.; Lopez-Arce, P. Silica nanoparticles (SiO<sub>2</sub>): Influence of relative humidity in stone consolidation. *J. Cult. Herit.* **2016**, *18*, 258–270. [[CrossRef](#)]
26. Peng, M.; Wang, L.; Guo, L.; Guo, J.; Zheng, L.; Yang, F.; Ma, Z.; Zhao, X. A Durable Nano-SiO<sub>2</sub>-TiO<sub>2</sub>/Dodecyltrimethoxysilane Superhydrophobic Coating for Stone Protection. *Coatings* **2022**, *12*, 1397. [[CrossRef](#)]
27. Ergenç, D.; Sierra-Fernandez, A.; Barbero-Barrera, M.d.M.; Gomez-Villalba, L.S.; Fort, R. Assessment on the performances of air lime-ceramic mortars with nano-Ca(OH)<sub>2</sub> and nano-SiO<sub>2</sub> additions. *Constr. Build. Mater.* **2020**, *232*, 117163. [[CrossRef](#)]
28. Zhang, X. Study on the migration and transformation mechanism of water and salt in tomb murals and the screening of common mural reinforcement materials. *Chang. Univ.* **2023**. [[CrossRef](#)]
29. Baltakys, K.; Jauberthie, R.; Siauciunas, R.; Kaminskas, R. Influence of modification of SiO<sub>2</sub> on the formation of calcium silicate hydrate. *Mater. Sci. Pol.* **2007**, *25*, 663–670.
30. Zaid, M.H.M.; Matori, K.A.; Ab, A.S.H.; Wahab, Z.A.; Rashid, S.S.A. Effect of sintering on crystallization and structural properties of soda lime silica glass. *Sci. Sinter.* **2017**, *49*, 409–417. [[CrossRef](#)]
31. Paradkar, M.; Irudayaraj, J. A rapid FTIR spectroscopic method for estimation of caffeine in soft drinks and total methylxanthines in tea and coffee. *J. Food Sci.* **2002**, *67*, 2507–2511. [[CrossRef](#)]
32. Rakić, V.M.; Hercigonja, R.V.; Dondur, V.T. CO interaction with zeolites studied by TPD and FTIR: Transition-metal ion-exchanged FAU-type zeolites. *Microporous Mesoporous Mater.* **1999**, *27*, 27–39. [[CrossRef](#)]
33. Obeidat, S.; Hammoudeh, A.; Alomary, A. Application of FTIR spectroscopy for assessment of green coffee beans according to their origin. *J. Appl. Spectrosc.* **2018**, *84*, 1051–1055. [[CrossRef](#)]
34. Liu, J.; Zhang, Q.-H.; Ma, F.; Zhang, S.-F.; Zhou, Q.; Huang, A.-M. Three-step identification of infrared spectra of similar tree species to *Pterocarpus santalinus* covered with beeswax. *J. Mol. Struct.* **2020**, *1218*, 128484. [[CrossRef](#)]
35. Meftah, N.; Mahboub, M.S. Spectroscopic characterizations of sand dunes minerals of El-Oued (Northeast Algerian Sahara) by FTIR, XRF and XRD analyses. *Silicon* **2020**, *12*, 147–153. [[CrossRef](#)]

**Disclaimer/Publisher’s Note:** The statements, opinions and data contained in all publications are solely those of the individual author(s) and contributor(s) and not of MDPI and/or the editor(s). MDPI and/or the editor(s) disclaim responsibility for any injury to people or property resulting from any ideas, methods, instructions or products referred to in the content.